Biosensors and Bioelectronics 149 (2020) 111843

Contents lists available at ScienceDirect

Biosensors and Bioelectronics

journal homepage: http://www.elsevier.com/locate/bios

CdS quantum dots/Au nanoparticles/ZnO nanowire array for self-powered photoelectrochemical detection of *Escherichia coli* O157:H7

Xiuxiu Dong [a,1], Zengliang Shi [a,1], Chunxiang Xu [a,*], Chi Yang [a,b], Feng Chen [a], Milan Lei [a], Junjie Wang [a], Qiannan Cui [a]

[a] State Key Laboratory of Bioelectronics, The National Demonstration Center for Experimental Biomedical Engineering Education, School of Biological Science and Medical Engineering, Southeast University, Nanjing, 210096, PR China

[b] Yale-NUIST Center on Atmospheric Environment, Nanjing University of Information Science and Technology, Nanjing, 210044, PR China

ARTICLE INFO

Keywords:
Self-powered
Photoelectrochemical
Aptasensor
E. coli O157:H7

ABSTRACT

In this paper, the hydrothermally grown ZnO nanowire array (NWs) was modified by Au nanoparticles (NPs) and CdS quantum dots (QDs) to construct a high-performance photoelectrochemical (PEC) electrode. The aligned ZnO NWs, which decorated Au NPs and CdS QDs have the effective light absorption range from UV to visible region. This hybrid structure provided a self-powered PEC electrode with a favorable energy-band configuration for fast charge separation and transportation. Meanwhile, the Au NPs and CdS QDs also made increase of the surface area to improve the immobilization of the analytes. After assembling aptamer as recognition element, this composite nanoarray was further developed as a self-powered PEC biosensor by synergizing above multiple enhancement factors. The PEC aptasensor exhibited a rapid response in a wide linear range of 10–10^7 CFU/mL with the detection limit as low as 1.125 CFU/mL to *Escherichia coli* O157:H7 (*E. coli* O157:H7). This approach would offer an alternative PEC transduction for fast environment monitoring and clinical diagnosis related to pathogenic bacteria.

1. Introduction

Pathogenic *Escherichia coli* O157:H7 (*E. coli* O157:H7) constitutes ongoing health concerns for women, newborns, elderly, and immunocompromised individuals due to increased amounts of urinary tract infections, newborn meningitis, abdominal sepsis, and septicemia (Mellata, 2013). These health threats have drawn a broad concern on *E. coli* detection. In the past few decades, gold-standard methods for pathogen detection, such as culturing the organisms on agar plates, were in demand among sanitary authorities. These methods are sensitive and low cost, but time-consuming because they require 48 h or even more to obtain confirmatory results which cannot meet the requirements of real-time detection (Zhang et al., 2018). Consequently, plenty of rapid methods have been developed, including flow cytometry (Hendrickson et al., 2019; McClain et al., 2001), polymerase chain reaction (PCR) (Laidlaw et al., 2019), and immunoassay, such as enzyme-linked immunosorbent assay, fluorescence immunoassay, electrochemical immunoassay, photoelectrochemical immunoassay and so on (Guner et al., 2017; Jijie et al., 2018; Liu et al., 2019b; Song et al., 2016; Xu et al., 2017; Yang et al., 2018; Zhang et al., 2017; Zhu et al., 2018). In these methods, flow cytometry and PCR techniques require trained professionals to operate the expensive equipment. Immunoassays such as enzyme-linked immunosorbent assay and fluorescence immunoassay cannot reach the required sensitivity because of the use of colorimetric detection. Among them, the emerging and fast-developing photoelectrochemical (PEC) sensing strategies have received considerable attention. Owing to the separation of the input (light) and output (electricity) signals, the PEC biosensor possesses a low background noise and an excellent sensitivity comparing to traditional electrochemical detection (Han et al., 2017).

Previously, the PEC method has been developed to detect the inactivation of *E. coli* (Kang et al., 2010; Nie et al., 2014; Yu et al., 2008). There are few PEC biosensors for trace detection of living *E. coli* (Hua et al., 2018), especially working at self-powered system without any external electrical supply. At zero bias voltage, the self-powered PEC sensor can effectively exclude the interferences from other reductive

* Corresponding author.
E-mail address: xcxseu@seu.edu.cn (C. Xu).
[1] These authors contributed equally: X. Dong, Z. Shi. Correspondence and requests for materials should be addressed to C. Xu xcxseu@seu.edu.cn.

https://doi.org/10.1016/j.bios.2019.111843
Received 24 August 2019; Received in revised form 25 October 2019; Accepted 1 November 2019
Available online 3 November 2019
0956-5663/

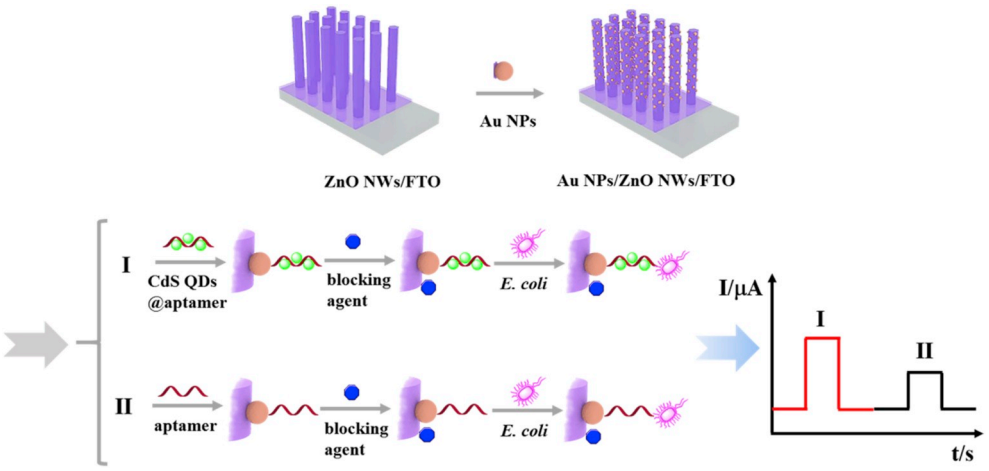

Fig. 1. Assembly process of the PEC biosensing for *E. coli* O157:H7. The process I states the PEC response based on aptamer/CdS QDs/Au NPs/ZnO NWs; process II states the PEC response based on aptamer/Au NPs/ZnO NWs as a control.

biomolecules in the detection system (Cakiroglu and Ozacar, 2019; Kang et al., 2015; Shang et al., 2019). The perfect design of photoelectrode material has become the main focus of PEC research because photoactive material can influence the intensity of photocurrent. Besides, retention of biological activity of biomolecule, especially for immunocomplex is also a critical evaluation basis for the nanomaterials in these biosensors' establishment. Due to its merits of high electron mobility, low toxicity, excellent biocompatibility, and high isoelectric point (Han et al., 2017; Liu et al., 2017), ZnO semiconductor has been applied in photodetector (Gupta et al., 2019), photoelectrochemical biosensor (Chen et al., 2019). Notably, the three-dimensional ZnO nanowire array (NWs) is quite suitable for PEC, for the reason that enlarged surface area is more in favor of electron transfer as well as enable facilitate the charge separation effectively (Liu et al., 2017). Besides, favorable energy-band alignment is important to a sensitive PEC biosensor. An effective strategy is introducing metal nanoparticle to enhance the absorption through surface plasmon resonance as well as assembling other semiconductors with matched energy band configuration. For examples, Au NPs (Dong et al., 2019), CdS (Hao et al., 2019b), CdSe (Li et al., 2019), and CdTe quantum dots (QDs) (Hao et al., 2019a)) have been used to enhance visible light absorption for improved photocatalysis (Wang et al., 2019a), electrochemical sensor (Li et al., 2018), optical sensors (Liu et al., 2019a), and biological imaging (Gu et al., 2018).

In our work, Au NPs and CdS QDs were assembled on the aligned ZnO nanowire to form a self-powered PEC platform with favorable energy band configuration and further developed into a sensitive aptasensor for *E. coli* by merging the nice electron transfer path of ZnO and the extended visible-light absorption and the localized surface plasmon of Au NPs. The PEC characters and biosensing performance were investigated, and the response mechanism was discussed in detail.

2. Experimental

2.1. Regents

The used oligonucleotides were synthesized and HPLC-purified by Sangon Biotech Co., Ltd (Shanghai, China) with the following sequences: aptamer probe of *E. coli* O157:H7 is 5′–SH–ATCCGTCACACCTGCTCTACTGGCCGGCTCAGCATGACTAAGA-AGGAAGTTATGTGGTGTTGGCTCCCGTAT-3'. Phosphate buffered saline (PBS, 0.01 mol/L) was obtained by mixing the 0.2 g KH_2PO_4, 2.9 g Na_2HPO_4•12 H_2O, 8.0 g NaCl, 0.2 g KCl. The pH values of PBS were adjusted by adding 1 mol/L HCl or NaOH. Ultrapure water obtained from a Millipore water purification system (18.25 MΩ*cm, Milli-Q, Millipore) was used in the assays. All reagents were of analytical reagent grade and were used without any further purification.

2.2. Apparatus

The morphologies of the samples were characterized using field emission scanning electron microscopy (FESEM, Carl Zeiss, Ultra Plus) and transmission electron microscope (TEM, FEI JEOL JEM-2100). The energy-dispersive X-ray spectroscopy (EDX, EX-250) was used to reveal elemental distribution of the composites equipped with FESEM. X-ray diffraction patterns were carried out on an Ultima IV (XRD, Japan) instrument using Cu Kα radiation source (λ = 1.54056 Å) to determine the crystal phase of the obtained samples. The UV–vis absorption spectra were performed on a Shimadzu UV-2450, Japan. The elemental composition of the samples were analyzed on a Thermo ESCALAB 250Xi X-ray photoelectron spectrometer by X-ray photoelectron spectroscopy (XPS) using monochromatic AlK Alpha radiation as the excitation source (Thermo Fisher Scientific, US).

2.3. Fabrication of the aptasensor

2.3.1. Synthesis of 3D zinc oxide nanowire array and gold nanoparticles

A seed layer of ZnO onto cleaned FTO substrates (resistivity 15 Ω/cm^2,0.5 cm × 1 cm, acquired from Luoyang Shangzhuo Technology, Ltd., China) was obtained by magnetron sputtering (High vacuum magnetron sputtering system, Shenyang scientific instrument co., LTD., Chinese academy of sciences; JGP-450) that referred to our previous work (Dong et al., 2019). Subsequently, the seeded FTO substrates were immersed in an aqueous solution of 25 mmol/L $Zn(CH_3COO)_2$•$2H_2O$ and equimolar $(CH_2)_6N_4$ and kept at 90 °C for 6 h to obtain ZnO nanowire array.

The synthesis of gold nanoparticles was referred to the previous method (Piella et al., 2016). 2.5 mL of $HAuCl_4$ (10 mmol/L), was injected into a reducing solution containing 150 mL of sodium citrate (SC, 2.2 mmol/L) and 0.1 mL of tannic acid (TA, 2.5 mmol/L) at 70 °C, the pH of the solution was additionally adjusted with 1 mL of potassium carbonate (K_2CO_3, 150 mmol/L) to ensure the solution remained at slightly alkaline values. After 5 min the reaction was finished. To further grow the seeds, the solution was diluted (1:3) by extracting 55 mL of the sample and adding 55 mL of SC 2.2 mmol/L. When the temperature reached again 70 °C, two subsequent injections of 1.25 mL of $HAuCl_4$ (10 mmol/L) were added. By subsequently repeating this process, dilution plus two injections, Au NPs were used after four injections in our experiment.

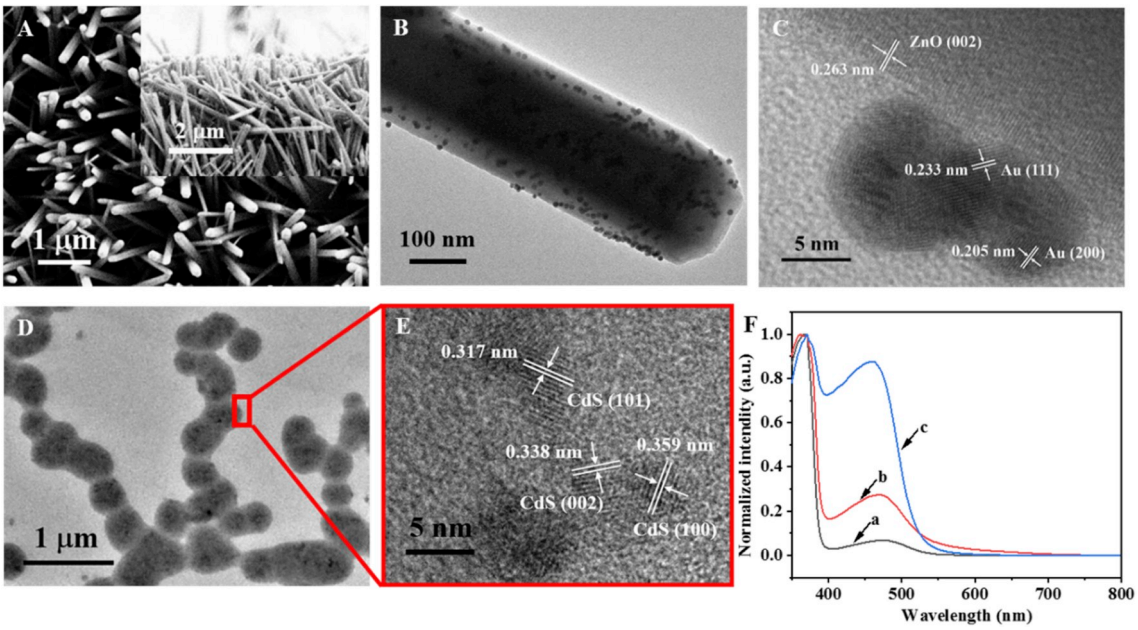

Fig. 2. (A) SEM images of ZnO NWs; (B) TEM image and (C) HRTEM image of Au NPs/ZnO NWs; (D) TEM image and (E) HRTEM of CdS QDs@ *E. coli* aptamer; (F) UV–vis spectra of (a) ZnO NWs, (b) Au NPs/ZnO NWs, (c) CdS QDs@*E. coli* aptamer/Au NPs/ZnO NWs.

2.3.2. Preparation of the CdS QDs@E. coli aptamer

CdS QDs@*E. coli* aptamer was prepared by in situ growth of CdS QDs on DNA chains according to the method reported previously (Dong et al., 2007; Li et al., 2018) with some modification. Briefly, 1 mL of 0.2 mmol/L $Cd(NO_3)_2$ was added to 1 mL of *E. coli* aptamer solution. The solution was mixed thoroughly and kept for 24 h at 4 °C. Then, 1 mL of 0.2 mmol/L Na_2S in water/ethanol (1:1, v/v) was added to this solution. The mixture was stirred thoroughly and incubated for a further 24 h at 4 °C. Then, 0.1 mL of 20 mmol/L aqueous $Cd(NO_3)_2$ was added and allowed to react for 24 h at 4 °C before introduction of 0.1 mL Na_2S (20 mmol/L) in water/ethanol (1:1, v/v). The solution was again incubated for 24 h at 4 °C. The as-obtained CdS QDs@*E. coli* aptamer nanochains were fairly stable and could be stored for more than 6 months at 4 °C without agglomeration.

2.3.3. Bacterial growth

E. coli O157:H7 and *S. aureus* grew in sterile Luria-Bertani (LB) media (2.0 g bacto-tryptone, 1.0 g bacto-yeast extract powder, 2.0 g NaCl dissolving in 200 mL distilled water, and adjusted to pH 7.4 with 3.0 mol/L NaOH) in an incubator-shaker at 37 °C to reach the growing stationary phase. After overnight incubation, 1 mL of bacterial cells was centrifuged (7000 rpm, 2 min) to remove the supernatant and washed 3 times with PBS (0.01 mol/L, pH 7.4), and resuspended in 1 mL of PBS. By plating bacteria on LB plates, the number of bacteria per milliliter can be acquired by counting related colony forming units (CFU) after incubation overnight at 37 °C.

In brief, the design principle of the amplified PEC biosensor of *E. coli* O157:H7 was shown in Fig. 1. Firstly, ZnO NWs were immersed in gold nanoparticles solution for 10 min and air-drying. Then Au NPs/ZnO NWs were incubated in 200 μL CdS QDs@*E. coli* aptamer solution at 37 °C for 60 min (process I in Fig. 1). And the unmodified *E. coli* aptamer was connected onto Au NPs/ZnO surface at the same condition as a control (process II in Fig. 1). Subsequently, to avoid nonspecific adsorption, 200 μL blocking reagent (5% BSA) was incubated at 37 °C for 60 min. For *E. coli* O157:H7 determination, the as-prepared aptasensors were immersed in different concentration *E. coli* O157:H7 solution at 37 °C for 100 min. After each step, the electrodes were completely rinsed and dried. At this point, the preparation of the bioelectrode is completed. And then the PEC measurements were performed with a homemade PEC system equipped with an Xe lamp with 350 nm cut-off filter (Mexe-500, Beijing NBET Technology Co., Ltd., China). The power density is 16 mW/cm^2. The photocurrent was measured on a CHI660D electrochemical workstation by using a standard three-electrode system: as-prepared photo-electrodes with an active area of 0.25 cm^2 were served as working electrodes with counter electrode of Pt net and reference electrode of Ag/AgCl. The photocurrent measurements were carried out at a constant potential of 0 V (vs Ag/AgCl), and 0.01 mol/L PBS (containing 0.1 mol/L ascorbic acid) was used as the supporting electrolyte for photocurrent measurements at room temperature.

3. Results and discussion

3.1. Characterization of the ZnO NWs, Au NPs, and CdS QDs@aptamer

The top view and cross-sectional view SEM images in Fig. 2A exhibit ordered and vertically-aligned grown ZnO nanowires on the FTO substrate. The diameter of ZnO NWs is about 130–200 nm, and the length of the nanowire is ~5 μm. The three-dimensional structure of ZnO can provide high specific surface area to harvest light. Moreover, large gap between each nanowire in ZnO NWs, which facilitates biomaterial assembly on the surface of ZnO furtherly. Loading the gold particles is effective approach to improve the photoelectrochemical performance due to its surface plasmon resonance. The TEM image in Fig. S1A displays distribution of gold particles with diameters of 6–9 nm, and Au NPs are evenly distributed on the surface of ZnO nanowire in Fig. 2B. As shown in Fig. 2C, the observed 0.263 nm lattice fringe of nanowire correspond to the (002) planes of the ZnO (JCPDS No.36–1451), 0.233 and 0.205 nm fringes of the nanoparticle correspond to the (111) and (200) planes of the Au, respectively (JCPDS No. 04–0784). The EDS spectra in Fig. S1B further present the element distribution of Zn, O, and Au, and indicate the uniform assembling of Au NPs on the ZnO NWs. The CdS QDs grow along the aptamer, and the complex structure is described in Fig. 2D. In Fig. 2E, the observed 0.359 nm, 0.338 nm, and 0.317 nm fringes of QDs correspond to the (100), (002) and (101) planes of the CdS (JCPDS No. 41–1049), respectively. Also, the UV–vis spectra of (a) ZnO NWs, (b) Au NPs/ZnO NWs, (c) CdS QDs@*E. coli* aptamer/Au NPs/ZnO NWs are observed in Fig. 2F. The improvement of light absorption

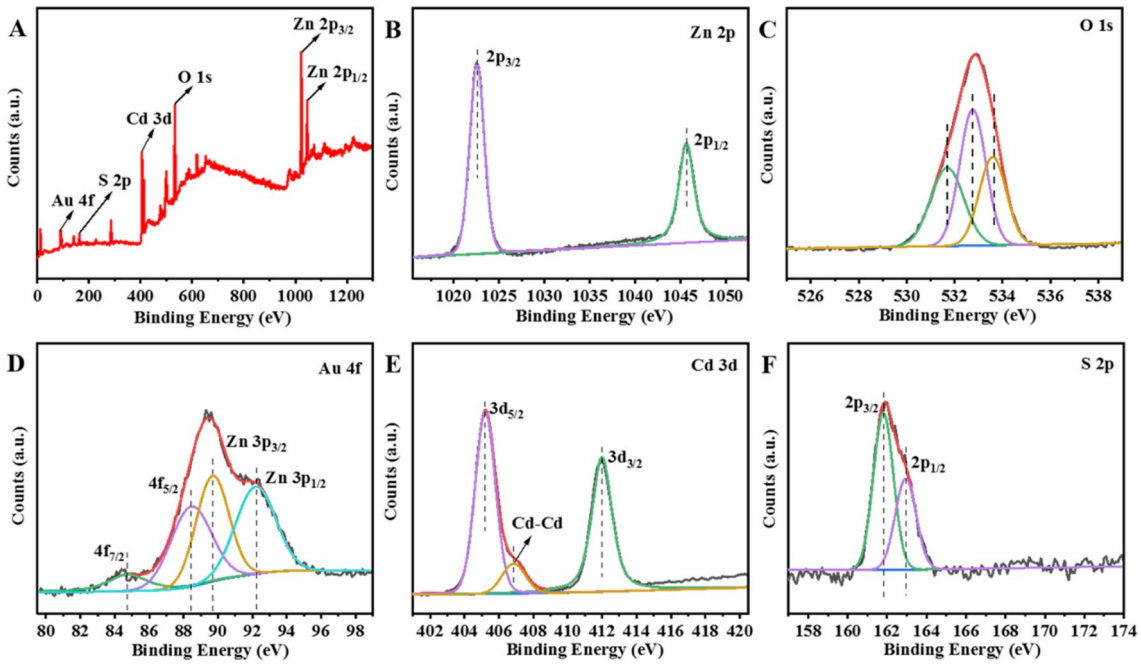

Fig. 3. XPS spectra of Cd/Au/ZnO. (A) Survey; (B) Zn 2p; (C) O 1s; (D) Au 4f and Zn 3p; (E) Cd 3d; (F) S 2p.

would bring enhancement of photocurrent.

The chemical composition and electronic structures of CdS/Au/ZnO were analyzed typically by XPS. The XPS survey spectrum shows the peaks of Zn, O, Au, Cd, and S elements as displayed in Fig. 3A, which demonstrate the formation of the CdS/Au/ZnO heterostructures. The Zn $2p_{3/2}$ and Zn $2p_{1/2}$ peaks for CdS/Au/ZnO (Fig. 3B) were at about 1022.5 and 1045.6 eV with a spin-orbit separation of 23.1 eV, which confirmed that Zn element existed mainly in the form of Zn^{2+} on the sample surface. As presented in Fig. 3C, the O 1s peak can be deconvoluted into three peaks at 531.6, 532.8 eV, and 533.6 eV, corresponding to oxygen ions in the wurtzite structure of ZnO, oxygen-deficient regions within the ZnO matrix, and the surface chemisorbed oxygen, respectively (Liang et al., 2018). The XPS spectrum of Au is complex because of its strong overlap with the peaks of Zn (Fig. 3D). Four peaks can be distinguished. Zn peaks of $3p_{3/2}$ and $3p_{1/2}$ contribute to the overlapped spectra and are located at around 89.6 eV and 92.1 eV,

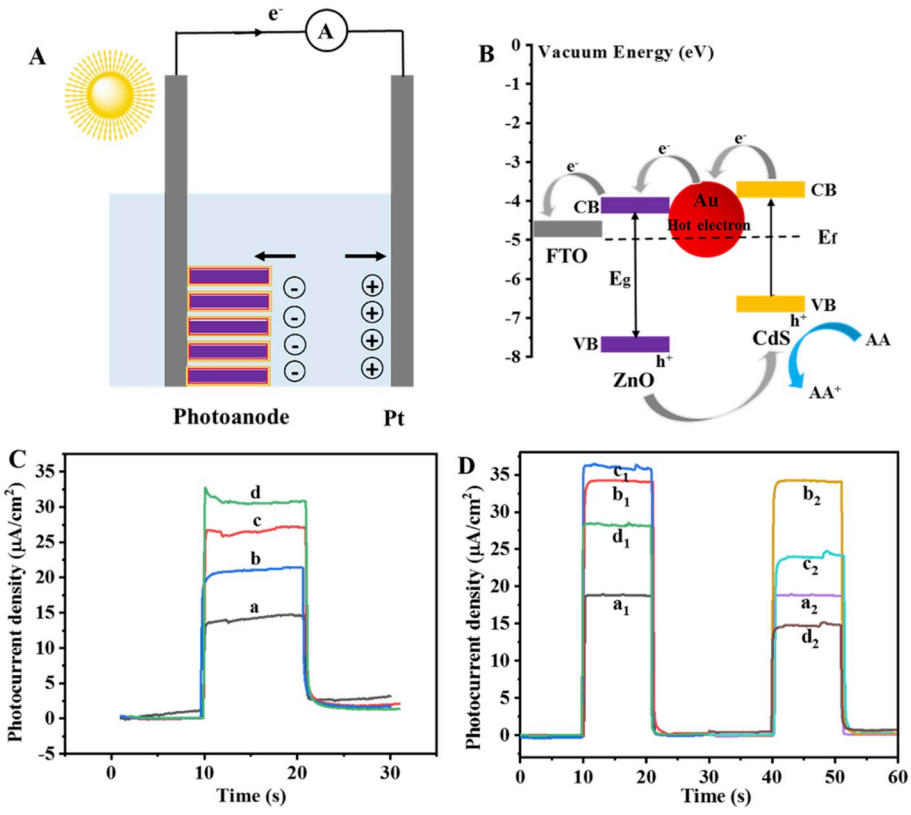

Fig. 4. Scheme of the device configuration (A), charge transfer process (B) in the CdS QDs/Au NPs/ZnO NWs electrode; (C) I-T curves. (a) ZnO NWs, (b) CdS QDs/ZnO NWs, (c) Au NPs/ZnO NWs, (d) CdS QDs/Au NPs/ZnO NWs; (D) the assembly process of PEC sensor based on CdS QDs/Au NPs/ZnO NWs and Au NPs/ZnO NWs: (a_1) ZnO NWs, (b_1) Au NPs/ZnO NWs, (c_1) CdS QDs@*E. coli* aptamer/Au NPs/ZnO NWs, (d_1) Blocking agent/CdS QDs@*E. coli* aptamer/Au NPs/ZnO NWs; (a_2) ZnO NWs, (b_2) Au NPs/ZnO NWs, (c_2) *E. coli* aptamer/Au NPs/ZnO NWs, (d_2) Blocking agent/*E. coli* aptamer/Au NPs/ZnO NWs.

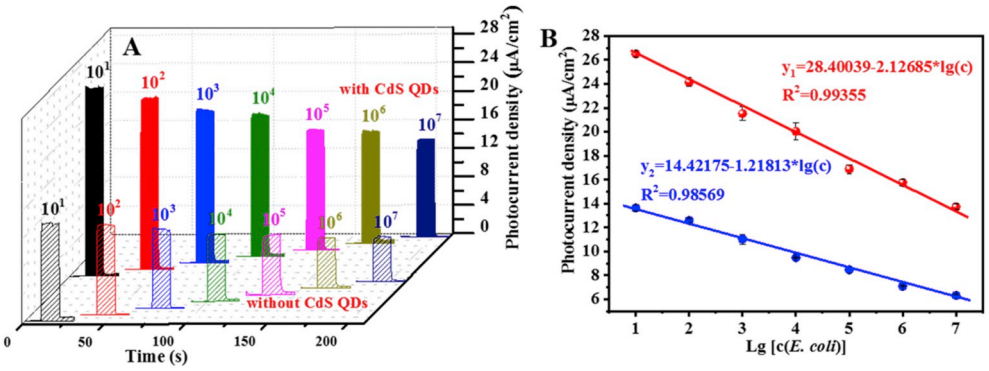

Fig. 5. I–T curves (A) and standard curves (B) of aptasensor for the detection of *E. coli* O157:H7: CdS QDs@ *E. coli* aptamer as an enhanced factor; without CdS QDs as a control.

respectively (Kwiatkowski et al., 2017). The Au $4f_{7/2}$ peak located at 84.7 eV is well separated apart from the others, so that its position can be determined precisely. As a consequence of spin-orbital splitting ($\Delta = 3.7$ eV), the second peak ($4f_{5/2}$) is observed at 88.4 eV. Comparison of the observed bond energy with the values reported for different Au compounds (Calzada et al., 2017) allows us to conclude that it corresponds to the metallic gold. The absence of any other peaks within 85–86 eV suggests that in our composites the gold exists only in the metallic state. The high-resolution XPS spectrum of the Cd orbital region (Fig. 3E) presented the binding energies of Cd $3d_{5/2}$ and Cd $3d_{3/2}$ peaks at 405.2 and 412.0 eV, respectively. The splitting energy of 6.8 eV between Cd $3d_{5/2}$ and Cd $3d_{3/2}$ was a typical value for Cd^{2+} in CdS (Wang et al. 2018, 2019b). Meanwhile, the peak at 406.9 eV is indexed to the binding energies of Cd $3d_{5/2}$, and attributed to the Cd–Cd energy states. The S 2p peak was fitted into two peaks (Fig. 3F). S 2p XPS peaks are also presented in Fig. 3F, two characteristic peaks at 161.8 and 162.9 eV in the ample were attributed to the doublet of S $2p_{3/2}$ and S $2p_{1/2}$, respectively (Yang et al., 2013; Zhao et al., 2015), indicating that the valence state of element S is −2. Findings from XPS analysis agree well with TEM and EDS results.

3.2. Feasibility of the aptasensor and charge transfer process

In the PEC system, the semiconductor plays a fundamental role in photoelectrode and some other materials further introduced to enhance or weaken the photocurrent response by changing the charge transfer (Sun et al., 2019; Zhang et al., 2019). For PEC biosensor, the photocurrent variation can reflect the concentration of analyte through assembly of biomolecules on the surface of electrode. To obtain the better sensitivity of aptasensor, it is effective to improve the initial photocurrent values. As shown in Fig. 4A, we use ZnO NWs as the template to produce a functionalized three-dimensional photoanode with gold nanoparticles. The CdS QDs were assembled to the Au NPs/ZnO NWs. The charge transfer process in the CdS QDs/Au NPs/ZnO NWs electrode can be described in Fig. 4B. In this configuration of CdS/Au/ZnO, the CdS and ZnO interface forms a type-II band alignment, where Au NPs act as an electron relay. The ZnO and CdS absorbed the photons and generated electron-hole pairs. The energetic electron transfers from conducting band of CdS QDs over the potential energy barrier of Au into ZnO that gold nanoparticles act as an electron relay (Guo et al., 2015; Li et al., 2015). In addition, Au NPs could strongly enhance the light absorption, facilitating the separation and transport of photoinduced charge through the effect of localized surface plasmon resonance (Zhao et al., 2018). The majority of the charges in ZnO transfer to the FTO glass while reduction of the photogenerated holes occurs at valence band of CdS with participation of ascorbic acid. This favorable energy-band alignment can bring good photoelectrochemical performance.

To verify the mechanism for the photocurrent response based on CdS/Au/ZnO structure, the photocurrent responses on ZnO, CdS/ZnO, Au/ZnO, and CdS/Au/ZnO are measured by photocurrent-time curves in Fig. 4C. Curve a is the PEC current of ZnO NWs with 14.5 μA. After coating the Au NPs on the ZnO electrode, the photocurrent density reaches 26.4 μA (curve c in Fig. 4C). Then, after CdS immobilization, the photocurrent further increases as 30.5 μA (curve d in Fig. 4C). At the same time, modifying the CdS QDs on the ZnO electrode was measured for comparison, the photocurrent density is 21.1 μA (curve b in Fig. 4C). These results indicate the synergistic effect of the CdS/Au/ZnO structure can induce a significant enhancement of photocurrent response.

To confirm the detection feasibility of our proposed PEC aptasensor, the photochemical measures of electrode assembly process were carried out in Fig. 4D. Curve a_1 is the PEC current of ZnO NWs with 18.8 μA. After coating the Au NPs on the ZnO electrode, the photocurrent density reaches to 34.3 μA (curve b_1 in Fig. 4D). The synergistic effect of the AuNPs/ZnO structure can provide a significant enhancement of the ZnO charge separation. Then, after CdS@*E. coli* aptamer immobilization, the photocurrent gradually increases as 36.2 μA (curve c_1 in Fig. 4D). Curve d_1 represents the electrode preparation completed after blocking agent immobilization with 28.2 μA. At the same time, the only *E. coli* aptamer is modified onto Au NPs/ZnO causing that the photocurrent decreases 23.9 μA (curve c_2 in Fig. 4D) and 14.6 μA after blocking agent immobilization. It indicates the immobilization of biomolecules hinders the electron transfer. However, the introduction of CdS QDs can reduce this hindrance. In brief, the PEC aptasensor for *E. coli* O157:H7 detection was well structured based on our earlier design.

3.3. Detection of E. coli O157:H7

Subsequently, the biosensing platform based on the CdS/Au/ZnO heterostructure was utilized to detect *E. coli* O157:H7 with various concentrations. The optimal detection conditions were investigated referred to our previous work (Dong et al., 2017). The optimal aptamer concentration is 250 μg/mL, the optimal incubation time for *E. coli* O157:H7 capture is 100 min, and the optimal pH of electrolyte is 7.4. The optimal AA concentration is 0.1 mol/L (Fig. S2). Fig. 5A shows I-T curves for the detection of *E. coli* using CdS QDs@*E. coli* aptamer and without CdS QDs. The peak current density decreases with the increase of *E. coli* concentration. As shown in Fig. 5B, the peak current density is linear with the common logarithm of *E. coli* concentration (c, CFU/mL) from 10 to 10^7 CFU/mL, with a linear regression equation of $y_1 = 28.40039–2.12685 \times \lg c$ ($R_1^2 = 0.99355$) for CdS QDs@*E. coli* aptamer-based aptasensor and $y_2 = 14.42175–1.21813 \times \log c$ ($R_2^2 = 0.98569$) for *E. coli* aptamer-based aptasensor. Besides, the limit of detection (LOD) was calculated referred to the method reported previously (Dong et al., 2017; Gan et al., 2016). To conclude, the LOD of this proposed aptasensor for the detection of *E. coli* O157:H7 is 1.125 CFU/mL (see supporting information). The LOD of the aptasensor without CdS QDs is 3.228 CFU/mL, which is higher than that of the aptasensor using CdS QDs@*E. coli* aptamer as enhanced factor. The

Table 1
Comparison of analytical methods for *E. coli* determination obtained in this study and that of previous reports by nanomaterials-based studies.

Methods	Nanomaterials	Linear range (CFU/mL)	Detection limit (CFU/mL)	References
Fluorescent sensor	carbon dots	1.0×10^5–1.0×10^8	9.5×10^4	Wang et al. (2016)
Fluorescent immunosensor	graphene quantum dots	–	1.0×10^2	Yang et al. (2018)
Colorimetric immunosensor	gold nanoparticle	5.0×10^1–5.0×10^4	5.0×10^1	Zheng et al. (2019)
Electrochemical immunosensor	CdS@ZIF-8	1.0×10^1–1.0×10^8	3	Zhong et al. (2019)
Electrochemical immunosensor	PPy/AuNP/MWCNT/Chi hybrid	3.0×10^1–3.0×10^7	3.0×10^1	Guner et al. (2017)
Electrochemical immunosensor	Au@Pt/SiO_2 NPs	3.5×10^2–3.5×10^8	1.83×10^2	Ye et al. (2018)
Photoelectrochemical ratiometric aptasensor	g-C_3N_4, C-dots/3DGH	2.9×10^0–2.9×10^6	–	Hua et al. (2018)
Photoelectrochemical aptasensor	CdS QDs/Au NPs/ZnO NWs	1.0×10^1–1.0×10^7	1.125	This work

sensitivity (slope of the regression curve) of the aptasensor using CdS QDs@*E. coli* aptamer as enhanced factor is 1.7 times that of the aptasensor without CdS QDs. The CdS QDs enhanced the generation of photo-electron, so the CdS QDs assembled aptasensor increased the photocurrent greatly. As a result, the I-T signals are amplified greatly by using CdS QDs@*E. coli* aptamer compared with the only *E. coli* aptamer. As listed in Table 1, the detection limit for the proposed photoelectrochemical detection of *E. coli* is much lower than that of the previous reports (typically higher than 30 CFU/mL). Moreover, our method is more sensitive than other reported methods.

3.4. Specificity, stability, and reproducibility of the aptasensor

The selectivity of the PEC aptasensor using CdS QDs@ *E. coli* aptamer as signal tags was studied in Fig. S3A (see supporting information). The bioelectrode shows a remarkable response to *E. coli* O157:H7 (1000 CFU/mL), but shows negligible responses to other pathogens and metal ions which coexist in the reaction system. These results indicate that the aptasensor has good selectivity toward the detection of *E. coli*, resulting from the specific interactions between the *E. coli* aptamer and surface antigen of *E. coli* cells.

To investigate the stability of the PEC aptasensor, the detection of *E. coli* O157:H7 (1000 CFU/mL) was conducted every 3 days for 15 days using 6 different bioelectrodes under the same conditions (Fig. S3B). After 15 days, the PEC aptasensor still retained 87% of its initial sensitivity. It is acceptable storage stability within 15 days. Also, the reproducibility of the sensor holds the key for its practical application. The proposed PEC aptasensor photocurrent responses were chronicled in 6 bioelectrodes after the incubation of *E. coli* O157:H7 (1000 CFU/mL). It can be observed from Fig. S3C, there was no difference in photocurrent response of 6 bioelectrodes, and the relative standard deviation (RSD) was about below 5%, indicating that the sensor has good reproducibility. Furthermore, we evaluated the recoveries by adding *E. coli* O157:H7 to the water samples. As shown in Table S1, satisfactory recoveries (86.54–109.1%) were achieved in water samples, indicating that the proposed aptasensor is available for detecting *E. coli* in real samples.

4. Conclusions

In summary, a self-powered PEC aptasensor capable of detecting *E. coli* O157:H7 was developed. The favorable energy-band alignment with effective and fast charge transport is constituted by well-aligned ZnO NWs, Au NPs as an electron relay and CdS QDs with a narrow bandgap. The elaborated PEC bioassay exhibited the apparent merits of low detection limit (1.125 CFU/mL), broad linear range (10–10^7 CFU/mL), excellent specificity and well stability. It was used for *E. coli* O157:H7 detection in water sample with satisfactory recoveries (86.54–109.1%). The PEC aptasensing platform can flexibly extend to monitor other targets by replacing the corresponding bio-recognition elements and thereby represents a versatile sensing protocol, which makes it a bright prospect in the area of bioanalysis.

Declaration of competing interest

The authors declare that they have no known competing financial interests or personal relationships that could have appeared to influence the work reported in this paper.

CRediT authorship contribution statement

Xiuxiu Dong: Conceptualization, Methodology, Investigation, Software, Writing - original draft. **Zengliang Shi:** Methodology, Investigation. **Chunxiang Xu:** Conceptualization, Methodology, Funding acquisition, Writing - review & editing, Supervision. **Chi Yang:** Writing - review & editing. **Feng Chen:** Validation. **Milan Lei:** Software. **Junjie Wang:** Investigation. **Qiannan Cui:** Validation, Supervision.

Acknowledgments

This work was supported by National Key Research and Development Program of China (2017YFA0700500, 2018YFA0209101), Science Fund for Creative Research Groups of the National Natural Science Foundation of China (61821002, 11734005, 61704024, 11604114, 91644103, 41603104), and Key research and development program of Jiangsu Province (BK20170696).

Appendix A. Supplementary data

Supplementary data to this article can be found online at https://doi.org/10.1016/j.bios.2019.111843.

References

Cakiroglu, B., Ozacar, M., 2019. A self-powered photoelectrochemical biosensor for H_2O_2, and xanthine oxidase activity based on enhanced chemiluminescence resonance energy transfer through slow light effect in inverse opal TiO_2. Biosens. Bioelectron. 141.

Calzada, L.A., Collins, S.E., Han, C.W., Ortalan, V., Zanella, R., 2017. Synergetic effect of bimetallic Au-Ru/TiO_2 catalysts for complete oxidation of methanol. Appl. Catal. B Environ. 207, 79–92.

Chen, Y.C., Yang, K.H., Huang, C.Y., Wu, Z.J., Hsu, Y.K., 2019. Overall photoelectrochemical water splitting at low applied potential over ZnO quantum dots/nanorods homojunction. Chem. Eng. J. 368, 746–753.

Dong, L.Q., Hollis, T., Connolly, B.A., Wright, N.G., Horrocks, B.R., Houlton, A., 2007. DNA-templated semiconductor nanoparticle chains and wires. Adv. Mater. 19 (13), 1748–1751.

Dong, X., Xu, C., Yang, C., Chen, F., Manohari, A.G., Zhu, Z., Zhang, W., Wang, R., You, D., Chen, J., 2019. Photoelectrochemical response to glutathione in Au-decorated ZnO nanorod array. J. Mater. Chem. C 7 (19), 5624–5629.

Dong, X.X., Yuan, L.P., Liu, Y.X., Wu, M.F., Liu, B., Sun, Y.M., Shen, Y.D., Xu, Z.L., 2017. Development of a progesterone immunosensor based on thionine-graphene oxide composites platforms: improvement by biotin-streptavidin-amplified system. Talanta 170, 502–508.

Gan, C.F., Ling, L., He, Z.Y., Lei, H.T., Liu, Y., 2016. In-situ assembly of biocompatible core-shell hierarchical nanostructures sensitized immunosensor for microcystin-LR detection. Biosens. Bioelectron. 78, 381–389.

Gu, D., Hong, L., Zhang, L., Liu, H., Shang, S.M., 2018. Nitrogen and sulfur co-doped highly luminescent carbon dots for sensitive detection of Cd (II) ions and living cell imaging applications. J. Photochem. Photobiol., B 186, 144–151.

Guner, A., Cevik, E., Senel, M., Alpsoy, L., 2017. An electrochemical immunosensor for sensitive detection of Escherichia coli O157:H7 by using chitosan, MWCNT, polypyrrole with gold nanoparticles hybrid sensing platform. Food Chem. 229, 358–365.

Guo, C.X., Xie, J.L., Yang, H.B., Li, C.M., 2015. Au@CdS core-shell nanoparticles-modified ZnO nanowires photoanode for efficient photoelectrochemical water splitting. Adv. Sci. 2 (12).
Gupta, S.P., Pawbake, A.S., Sathe, B.R., Late, D.J., Walke, P.S., 2019. Superior humidity sensor and photodetector of mesoporous ZnO nanosheets at room temperature. Sens. Actuators B Chem. 293, 83–92.
Han, Z.Z., Luo, M., Chen, L., Pan, H.B., Chen, J.H., Li, C.Y., 2017. A photoelectrochemical biosensor for determination of DNA based on flower rod-like zinc oxide heterostructures. Microchim Acta 184 (8), 2541–2549.
Hao, N., Lu, J.W., Chi, M.J., Xiong, M., Zhang, Y., Hua, R., Wang, K., 2019. A universal photoelectrochemical biosensor for dual microRNA detection based on two CdTe nanocomposites. J. Mater. Chem. B 7 (7), 1133–1141.
Hao, X.Q., Hu, Y., Cui, Z.W., Zhou, J., Wang, Y., Zou, Z.G., 2019. Self-constructed facet junctions on hexagonal CdS single crystals with high photoactivity and photostability for water splitting. Appl. Catal. B Environ. 244, 694–703.
Hendrickson, O.D., Nikitushkin, V.D., Zherdev, A.V., Dzantiev, B.B., 2019. Lectin-based detection of Escherichia coli and Staphylococcus aureus by flow cytometry. Arch. Microbiol. 201 (3), 313–324.
Hua, R., Hao, N., Lu, J.W., Qian, J., Liu, Q., Li, H.N., Wang, K., 2018. A sensitive Potentiometric resolved ratiometric Photoelectrochemical aptasensor for Escherichia coli detection fabricated with non-metallic nanomaterials. Biosens. Bioelectron. 106, 57–63.
Jijie, R., Kahlouche, K., Barras, A., Yamakawa, N., Bouckaert, J., Gharbi, T., Szunerits, S., Boukherroub, R., 2018. Reduced graphene oxide/polyethylenimine based immunosensor for the selective and sensitive electrochemical detection of uropathogenic Escherichia coli. Sens. Actuators B Chem. 260, 255–263.
Kang, Q., Lu, Q.Z., Liu, S.H., Yang, L.X., Wen, L.F., Luo, S.L., Cai, Q.Y., 2010. A ternary hybrid CdS/Pt-TiO2 nanotube structure for photoelectrocatalytic bactericidal effects on Escherichia Coli. Biomaterials 31 (12), 3317–3326.
Kang, Z., Gu, Y.S., Yan, X.Q., Bai, Z.M., Liu, Y.C., Liu, S., Zhang, X.H., Zhang, Z., Zhang, X.J., Zhang, Y., 2015. Enhanced photoelectrochemical property of ZnO nanorods array synthesized on reduced graphene oxide for self-powered biosensing application. Biosens. Bioelectron. 64, 499–504.
Kwiatkowski, M., Chassagnon, R., Geoffroy, N., Herbst, F., Heintz, O., Bezverkhyy, I., Skompska, M., 2017. Enhancement of visible light photoelectrocatalytic activity of ZnO (core)/TiO_2(shell) composite by N-doping and decorating with Au-0 nanoparticles. Electrochim. Acta 246, 213–225.
Laidlaw, A.M., Ganzle, M.G., Yang, X.Q., 2019. Comparative assessment of qPCR enumeration methods that discriminate between live and dead Escherichia coli O157:H7 on beef. Food Microbiol. 79, 41–47.
Li, C., Zhu, X.T., Zhang, H.F., Zhu, Z.C., Liu, B., Cheng, C.W., 2015. 3D ZnO/Au/CdS sandwich structured inverse opal as photoelectrochemical anode with improved performance. Adv Mater Interfaces 2 (18).
Li, F.L., Guo, Y.M., Wang, X.Y., Sun, X., 2018. Multiplexed aptasensor based on metal ions labels for simultaneous detection of multiple antibiotic residues in milk. Biosens. Bioelectron. 115, 7–13.
Li, P.P., Liu, X.P., Mao, C.J., Jin, B.K., Zhu, J.J., 2019. Photoelectrochemical DNA biosensor based on g-C3N_4/MoS_2 2D/2D heterojunction electrode matrix and co-sensitization amplification with CdSe QDs for the sensitive detection of ssDNA. Anal. Chim. Acta 1048, 42–49.
Liang, S.J., Han, B., Liu, X.M., Chen, W.Y., Peng, M., Guan, G.J., Deng, H., Lin, Z., 2018. 3D spatially branched hierarchical Z-scheme CdS-Au nanoclusters-ZnO hybrids with boosted photocatalytic hydrogen evolution. J. Alloy. Comp. 754, 105–113.
Liu, A.R., Yin, K.F., Mi, L., Ma, M.Y., Liu, Y.J., Li, Y., Wei, W., Zhang, Y.J., Liu, S.Q., 2017. A novel photoelectrochemical immunosensor by integration of nanobody and ZnO nanorods for sensitive detection of nucleoside diphosphatase kinase-A. Anal. Chim. Acta 973, 82–90.
Liu, C.H., Qiu, Y.Y., Zhang, J., Liang, Q., Mitsuzaki, N., Chen, Z.D., 2019. Construction of CdS quantum dots modified g-C_3N_4/ZnO heterostructured photoanode for efficient photoelectrochemical water splitting. J. Photochem. Photobiol., A 371, 109–117.
Liu, D.Q., Li, T.C., Huang, W.C., Ma, Z., Zhang, W., Zhang, R., Yan, H., Yang, B., Liu, S.Q., 2019. Electrochemiluminescent detection of Escherichia coli O157:H7 based on Ru(bpy)(3)(2+)/ZnO nanorod arrays. Nanotechnology 30 (2).
McClain, M.A., Culbertson, C.T., Jacobson, S.C., Ramsey, J.M., 2001. Flow cytometry of Escherichia coli on nucrifluidic devices. Anal. Chem. 73 (21), 5334–5338.
Mellata, M., 2013. Human and avian extraintestinal pathogenic Escherichia coli: infections, zoonotic risks, and antibiotic resistance trends. Foodb. Pathog. Dis. 10 (11), 916–932.
Nie, X., Li, G.Y., Wong, P.K., Zhao, H.J., An, T.C., 2014. Synthesis and characterization of N-doped carbonaceous/TiO_2 composite photoanodes for visible-light photoelectrocatalytic inactivation of Escherichia coli K-12. Catal. Today 230, 67–73.
Piella, J., Bastus, N.G., Puntes, V., 2016. Size-controlled synthesis of sub-10-nanometer citrate-stabilized gold nanoparticles and related optical properties. Chem. Mater. 28 (4), 1066–1075.
Shang, M.X., Zhang, J.L., Qi, H., Gao, Y., Yan, J.Y., Song, W.B., 2019. All-electrodeposited amorphous MoSx@ZnO core-shell nanorod arrays for self-powered visible-light-activated photoelectrochemical tobramycin aptasensing. Biosens. Bioelectron. 136, 53–59.
Song, C.M., Liu, C., Wu, S.Y., Li, H.L., Guo, H.Q., Yang, B., Qiu, S., Li, J.W., Liu, L., Zeng, H.J., Zhai, X.Z., Liu, Q., 2016. Development of a lateral flow colloidal gold immunoassay strip for the simultaneous detection of Shigella boydii and Escherichia coli O157:H7 in bread, milk and jelly samples. Food Control 59, 345–351.
Sun, B., Dong, J., Cui, L., Feng, T.T., Zhu, J.J., Liu, X.H., Ai, S.Y., 2019. A dual signal-on photoelectrochemical immunosensor for sensitively detecting target avian viruses based on AuNPs/g-C_3N_4 coupling with CdTe quantum dots and in situ enzymatic generation of electron donor. Biosens. Bioelectron. 124, 1–7.
Wang, B.Y., Peng, F., Yang, S.Y., Cao, Y.H., Wang, H.J., Yu, H., Zhang, S.Q., 2018. Hydrogenated CdS nanorods arrays/FTO film: a highly stable photocatalyst for photocatalytic H-2 production. Int. J. Hydrogen Energy 43 (37), 17696–17707.
Wang, G.Z., Long, X.J., Qi, K.Z., Dang, S.H., Zhong, M.M., Xiao, S.Y., Zhou, T.W., 2019. Two-dimensional CdS/g-C_6N_6 heterostructure used for visible light photocatalysis. Appl. Surf. Sci. 471, 162–167.
Wang, L., Gao, Z., Li, Y., She, H., Huang, J., Yu, B., Wang, Q., 2019. Photosensitization of CdS by acid red-94 modified alginate: dual ameliorative effect upon photocatalytic hydrogen evolution. Appl. Surf. Sci. 492, 598–606.
Wang, N., Wang, Y.T., Guo, T.T., Yang, T., Chen, M.L., Wang, J.H., 2016. Green preparation of carbon dots with papaya as carbon source for effective fluorescent sensing of Iron (III) and Escherichia coli. Biosens. Bioelectron. 85, 68–75.
Xu, M., Wang, R.H., Li, Y.B., 2017. Electrochemical biosensors for rapid detection of Escherichia coli O157:H7. Talanta 162, 511–522.
Yang, G.R., Yan, W., Zhang, Q., Shen, S.H., Ding, S.J., 2013. One-dimensional CdS/ZnO core/shell nanofibers via single-spinneret electrospinning: tunable morphology and efficient photocatalytic hydrogen production. Nanoscale 5 (24), 12432–12439.
Yang, X.Z., Feng, L.Q., Qin, X., 2018. Preparation of the Cf-GQDs-Escherichia coli O157: H7 bioprobe and its application in optical imaging and sensing of Escherichia coli O157: H7. Food Anal Method 11 (8), 2280–2286.
Ye, L.X., Zhao, G.Y., Dou, W.C., 2018. An electrochemical immunoassay for Escherichia coli O157:H7 using double functionalized Au@Pt/SiO_2 nanocomposites and immune magnetic nanoparticles. Talanta 182, 354–362.
Yu, H., Quan, X., Zhang, Y., Ma, N., Chen, S., Zhao, H., 2008. Electrochemically assisted photocatalytic inactivation of Escherichia coli under visible light using a $ZnIn_2S_4$ film electrode. Langmuir 24 (14), 7599–7604.
Zhang, J., Song, X.H., Xiong, Z.B., Dong, H.F., Wang, W.C., Chen, Z.D., 2017. Nanogold/Bi_2S_3 nanorods catalyzed silver deposition for carbon nanohorns-enhanced electrochemical immunosensing of Escherichia coli O157:H7. J. Electrochem. Soc. 164 (9), H572–H578.
Zhang, J.L., Wang, J.J., Zhang, X.Q., He, F.J., 2018. Rapid detection of Escherichia coli based on 16S rDNA nanogap network electrochemical biosensor. Biosens. Bioelectron. 118, 9–15.
Zhang, Y.F., Wang, M.D., Wang, Y.G., Feng, J.H., Zhang, Y., Sun, X., Du, B., Wei, Q., 2019. Label-free photoelectrochemical immunosensor for amyloid beta-protein detection based on SnO_2/$CdCO_3$/CdS synthesized by one-pot method. Biosens. Bioelectron. 126, 23–29.
Zhao, H., Dong, Y., Jiang, P., Wang, G., Miao, H., Wu, R., Kong, L., Zhang, J., Zhang, C., 2015. Light-Assisted preparation of a ZnO/CdS nanocomposite for enhanced photocatalytic H_2 evolution: an insight into importance of in situ generated ZnS. ACS Sustain. Chem. Eng. 3 (5), 969–977.
Zhao, Y., Gong, J., Zhang, X.B., Kong, R.M., Qu, F.L., 2018. Enhanced biosensing platform constructed using urchin-like ZnO-Au@CdS microspheres based on the combination of photoelectrochemical and bioetching strategies. Sens. Actuators B Chem. 255, 1753–1761.
Zheng, L.Y., Cai, G.Z., Wang, S.Y., Liao, M., Li, Y.B., Lin, J.H., 2019. A microfluidic colorimetric biosensor for rapid detection of Escherichia coli O157:H7 using gold nanoparticle aggregation and smart phone imaging. Biosens. Bioelectron. 124, 143–149.
Zhong, M., Yang, L., Yang, H., Cheng, C., Deng, W., Tan, Y., Xie, Q., Yao, S., 2019. An electrochemical immunobiosensor for ultrasensitive detection of Escherichia coli O157:H7 using CdS quantum dots-encapsulated metal-organic frameworks as signal-amplifying tags. Biosens. Bioelectron. 126, 493–500.
Zhu, F.J., Zhao, G.Y., Dou, W.C., 2018. Electrochemical sandwich immunoassay for Escherichia coli O157:H7 based on the use of magnetic nanoparticles and graphene functionalized with electrocatalytically active Au@Pt core/shell nanoparticles. Microchim Acta 185 (10).